Scale Effects on Cavitation on a Hydrofoil

(article starts on next page)

Scale Effects on Cavitation on a Hydrofoil

Qais Khraisat,[1] **Martin Persson,**[2] **Marko Vikström,**[2] **and Rickard E. Bensow**[1]

[1]Department of Mechanics and Maritime Sciences, Chalmers University of Technology, Gothenburg, Sweden
[2]Kongsberg Hydrodynamic Research Center, Kristinehamn, Sweden

ABSTRACT

In this work, a study on the scale effects on cavitation for the TU Delft Twist 11 hydrofoil is presented. The numerical simulations were performed with RANS, and cavitation is modeled by the mixture approach with the Schnerr-Sauer mass transfer model. Results are validated with model scale experimental data provided by TU Delft and EPFL. The numerical predictions show that scale effects have an influence on the cavity length, shedding behavior, vortical structures, and the re-entrant jet. In comparison with model scale observations, the attached cavity length extends further in the downstream direction. In addition, the vortical structures appear weaker at full scale which initiates intermittent cavities that collapse at an earlier stage during a shedding cycle relative to model scale. Analysis of the re-entrant jet shows different behaviors at model and full scales, which has been attributed to the jet momentum and how it travels to the leading edge. In addition, the possibility of using wall function at full scale is studied and shows promising results when compared with the results of the wall resolved approach.

Keywords Scale effects; RANS; Cavitation; Cloud shedding; Re-entrant jet

1 INTRODUCTION

A generic definition of cavitation is the development of vapor within the liquid medium at which the local static pressure drops below the saturation threshold. In the case of marine propellers and hydrofoils, it has adverse effects on performance, vibration, erosion, and noise. Depending on the operating condition, mainly angle of attack and cavitation number, one or several forms of cavity patterns may develop (Franc & Michel, 1985). However, only certain types are considered harmful and that is when the cavity behaves dynamically with transient growth and collapse. Bark *et al.* (2009) classified erosive cavitation to fall into five categories. It includes isolated traveling bubbles, the shedding of an attached cavity due to a re-entrant jet, secondary cavities that develop by flow and pressure fields, a detached cavity due to a change in condition, and the collapse of an attached/ sheet structure.

In the case of the TU Delft Twist 11 hydrofoil, the observed cavitation behavior falls within the second and third categories as a periodic shedding behavior of the attached cavity occurs. This is attributed to the re-entrant jet flowing upstream to the leading edge and the shear interaction with the external flow (Foeth, 2008). As the detached cavity/cloud is transported downstream, secondary vortical cavitation structures develop as well. This test case was introduced as a benchmark study during the workshop at the Second International Symposium on Marine Propulsors. The purpose of introducing the benchmark test case was to compare the results of involved participants and evaluate different numerical approaches. Bensow (2011) performed simulations using RANS, DES, and LES techniques. A better agreement with the experiments and more flow structures are resolved with the LES approach, while a lack in the shedding mechanisms is found with RANS. Similar conclusions were drawn by Whitworth (2011) when comparing DES and RANS results. Maquil *et al.* (2011) studied the case with the RANS approach, and expressed "a fair level of predictive agreement with experimental observations". Since then, work has been published on the test case studying various topics such as grid resolution requirements (Asnaghi *et al.*, 2018), the influence of leading edge roughness (Asnaghi & Bensow, 2020), and cavitation erosion (Wang *et al.*, 2023).

In this work, a study on the scale effects on cavitation with the RANS approach is performed. The main reason behind the choice of the RANS method rather than a scale resolving approach is the anticipated requirement for spatial resolution when dealing with high Reynolds number flows which yields to an unfeasible computational time. The objectives are to gain insights into how the cavity behavior changes in comparison with model scale observations and to perform a systematic grid study to understand resolution requirements for such cases.

2 TEST CASE

The test case chosen to achieve those objectives is the TU Delft Twist 11 foil. The hydrofoil geometrical profile is based on the NACA0009 with a chord length of $C = 150$ mm and a span of $S = 300$ mm. The geometry was developed with a symmetric varying angle of attack in the spanwise direction from 0 deg on the sides up to 11 deg at the centerline. The reasoning behind the design choice is to create a loading variation on the foil and to initiate a three-dimensional cavity. To diminish the influence of a developing laminar boundary layer on the cavity formation,

rough elements were applied to the leading edge of the hydrofoil. The roughness height is estimated to be 120 μm, and covers up to 4% of the chord length. The tests were conducted at the cavitation tunnels of TU Delft University of Technology and École Polytechnique Fédérale de Lausanne (EPFL). Note that the tests at EPFL were performed on a hydrofoil at a smaller geometrical scale. In this paper, the numerical set-up is a representation of the TU Delft test for wetted and cavitating conditions at an angle of attack -2 deg.

3 NUMERICAL SETUP

3.1 Computational Domain and Boundary Conditions
The computational domain is created based on the recommendations outlined for the workshop. The foil is placed 2 chord lengths from the inlet to the leading edge, and 4 chord lengths from the trailing edge to the outlet as shown in Figure 1. Slip wall boundary conditions are applied to the tunnel side, top, and bottom walls. To reduce the computation time, only half of the foil is considered with a symmetry boundary condition imposed at the centerline plane of the tunnel. The foil is modeled with no-slip wall boundary condition, and roughness is applied to the leading edge to mimic the experiments. The implemented roughness function is based on Schultz & Flack (2007) with constants $k^+_{smooth} = 3$, $k^+_{rough} = 15$, and $C_s = 0.26$. Considering that the mass transfer is pressure driven, it expected that the roughness model will not affect cavitation inception. Fixed velocity inlet and pressure outlet boundary conditions are applied. Since the objective is to study the scale effects on cavitation, a geometrically scaled model is created with a scaling ratio $\lambda = 20$ and will be referred to as "full scale". Wetted and cavitating simulations are performed for both model and full scales.
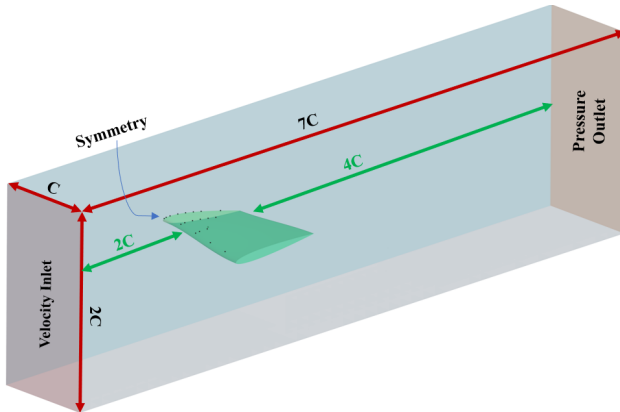

Figure 1: Domain and boundary conditions

At model scale, the tunnel has a fixed inflow condition of 6.97 m/s. Under the cavitating condition, the domain has been depressurized to a reference pressure level of 29 kPa. This matches the experimental cavitation number of $\sigma = 1.07$. Based on these conditions, the foil operates with a Reynolds number of $Re = 1.1 \times 10^6$.

The full scale simulations are performed on a geometrically scaled foil as mentioned previously. The non-dimensional

cavitation number is maintained the same as that of the model scale condition by adjusting the pressure. However, Reynolds number has increased to $Re = 2.6 \times 10^7$. Such condition for Re is chosen based on typical full scale marine propeller operation. It is worth noting that water and vapor properties are the same for both scales which match the provided values in the workshop.
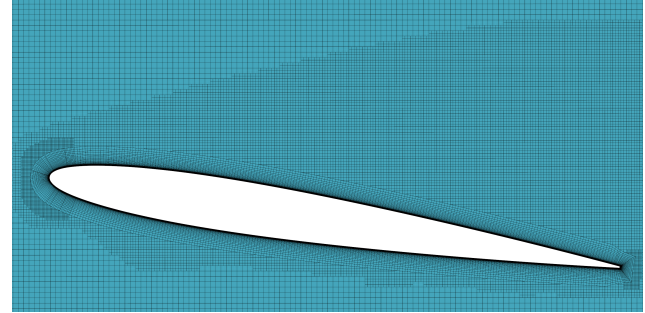

Figure 2: Grid at the symmetry plane

3.2 Grid Generation and Numerical Method
The grids are generated using the commercial software package Simcenter STAR-CCM+ 2022.1.1 with the built-in trimmer mesher which is predominantly hexahedral cells. Three grids are created for each of the cases with an additional one to study the influence of wall function (G4) at full scale as shown in Tables 1 and 2. The grid refinement is performed following the outlined procedure for unstructured meshes (Crepier, 2017) to generate as geometrically similar grids as possible. In addition, the suction side grid resolution is similar for each corresponding grid at model and full scale conditions. For example, note that the number of suction side surface cells for G3 is approximately 53.8×10^3 at both model and full scales. Furthermore, to ensure a smooth transition from the last prism layer and the volume mesh, approximately 1 : 1 ratio is maintained in this region.

Table 1: Generated grids for the model scale condition

	G1	G2	G3
Cell count (millions)	1.9	5.7	12.8
Suction side surface cells	14,891	31,403	53,829
Prism layers	24	36	48
Prism growth ratio	1.3	1.19	1.14
Mean y^+	0.54	0.36	0.26

Table 2: Generated grids for the full scale condition

	G1	G2	G3	G4
Cell count (millions)	2.2	6.7	15.3	4.0
Suction side surface cells	14,820	31,032	53,863	31,101
Prism layers	34	51	68	20
Prism growth ratio	1.3	1.19	1.14	1.19
Mean y^+	0.6	0.41	0.29	96

The boundary layer is resolved for all grids, except G4, by ensuring the non-dimensional mean value of y^+ of 0.6 or less. The additional grid G4 is generated for the full scale

case to evaluate the performance of using wall function for such cases, hence a mean $y^+ = 96$. The all y^+ wall treatment is used in all the cases.

To model cavitation, the single fluid approach is used which treats the liquid and vapor as one homogeneous mixture. The flow is assumed to be incompressible and the mixture density varies depending on the local volume fraction α. This means that the continuity and momentum equations are solved for the mixture rather than for each phase. The mixture density and dynamic viscosity are defined by,

$$\rho_m = \alpha_v \rho_v + (1 - \alpha_v)\rho_l, \tag{1}$$

$$\mu_m = \alpha_v \mu_v + (1 - \alpha_v)\mu_l, \tag{2}$$

where subscripts m, v, and l denote mixture, vapor, and liquid. ρ is the density, α is the volume fraction, and μ is the dynamic viscosity.

Since two phases will occupy the domain, only one additional transport equation is needed to solve for the volume fraction α,

$$\frac{\partial \alpha}{\partial t} + \nabla(\alpha u) = \frac{\dot{m}}{\rho}, \tag{3}$$

where $\dot{m}$ is the mass transfer rate source term for vaporization and condensation. In the literature, a few mass transfer models have been proposed and studied. In this work, the Schnerr-Sauer model is used which is a simplified version of the Rayleigh-Plesset equation (Schnerr & Sauer, 2001). Viscous effects, bubble growth acceleration, surface tension, and slip between vapor bubbles and liquid are all neglected. The mass transfer source term can be obtained as,

$$\alpha_v = \frac{V_v}{V_{cell}} = \frac{n_0 \frac{4}{3}\pi R^3}{1 + n_0 \frac{4}{3}\pi R^3}, \tag{4}$$

$$\frac{d\alpha_v}{dt} = \alpha_v(1 - \alpha_v)\frac{3}{R}\frac{dR}{dt}, \tag{5}$$

$$\frac{dR}{dt} = \sqrt{\frac{2}{3}\frac{|P(R) - P_\infty|}{\rho_l}}, \tag{6}$$

$$\dot{m} = \begin{cases} C_c \frac{\rho_l \rho_v}{\rho_m}\frac{d\alpha_v}{dt} & \max(P(R) - P_v, 0) \\ \\ C_v \frac{\rho_l \rho_v}{\rho_m}\frac{d\alpha_v}{dt} & \min(P(R) - P_v, 0) \end{cases} \tag{7}$$

The initial number of bubbles per unit volume of liquid n_0 and diameter are set 10^{12} m^{-3} and 10^{-6} m, respectively. While tuning parameters relating to bubble density and diameter of the mass transfer model may influence the predicted cavity, this analysis is not performed due to computational and timeline limitations. Also, the condensation C_c and vaporization terms C_v have both been set to 1.0, which is the default setting in the code.

The Reynolds-averaged Navier-Stokes (RANS) approach is used to run the simulations. Turbulence is modeled with the $k - \omega\ SST$ model (Menter et al., 2003) which uses the strain rate S to calculate the eddy viscosity μ_T as,

$$\mu_T = \frac{\rho k}{\min(\frac{a^*}{\omega}, \frac{a_1}{SF_2})}, \tag{8}$$

where ρ is the density, a_1 and a^* are model constants, k is the turbulent kinetic energy, ω is the specific dissipation rate, and F_2 is a blending function.

In cases of multiphase flows (cavitation), it has been shown that the eddy viscosity models tend to predict high turbulent viscosity near the cavity closure (Reboud et al., 1998; Coutier et al., 2003; Bensow, 2011). As a result, this will prevent the formation of the re-entrant jet and it will not travel underneath the cavity and upstream to the leading edge. In the case of the TU Delft Twist 11 foil, the shedding behavior of the cavity is mainly dependent on the re-entrant jet, therefore, a correction is needed. A proposed idea to reduce the turbulent viscosity for such cases is shown in the equation below which was developed empirically, and is known as the Reboud correction (Reboud et al., 1998),

$$f(\rho) = \rho_v + \left(\frac{\rho_v - \rho}{\rho_v - \rho_l}\right)^n (\rho_l - \rho_v), \tag{9}$$

where n is a constant and is set to the recommended value of 10. It is worth mentioning that this correction for the eddy viscosity is only active in the mixture regions.

Steady-state simulations were performed for the wetted flow condition, and the solution was subsequently used to initialize the unsteady cavitating flow simulations. All unsteady simulations were performed at a time step level of $\Delta t = 3 \times 10^{-5}$ s, which results to a mean CFL < 0.1 for both model and full scale conditions.

4 RESULTS AND DISCUSSION

4.1 Wetted Flow Condition

Results of the predicted pressure coefficient $-C_p$ distribution are shown in Figure 3 for 40% and 50% of the total spanwise length. The y-axis shows the non-dimensional pressure coefficient, and the x-axis shows the non-dimensional chord length. As all grids predict similar pressure distributions, and to avoid cluttering, the results are presented only for simulations of the finest grids G3, the grid with wall function G4, and the experimental data from the TU Delft and EPFL tests.

The numerical results show good agreement with the experimental measurements. A slight underprediction relative to the TU Delft data is present, but a better match with the EPFL test is obtained. Comparing the numerically predicted pressure distribution for both scales, similar levels are obtained. Even when using the wall function, the relative difference to the finest grid is on average approximately 0.5%. Such difference is minor and indicates that the wall function seems to give good results under wetted flow conditions for such case.

Table 3 shows the lift coefficient for all grids at both model and full scale. Minor differences for the predicted C_L are obtained when comparing the results for the different grid resolutions. This is expected based on the predicted pressure distribution as it is the dominant component for lift. The relative difference to the experimental measurement is at an acceptable range approximately -3% at model scale. On the other hand, the lift coefficient at full scale shows a better agreement to the experiment. This means that with
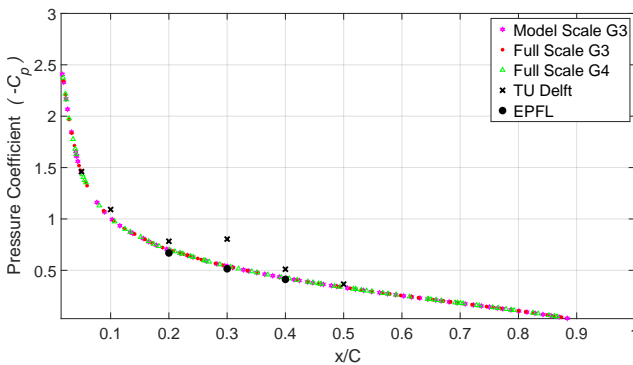
the non-dimensional similarities, i.e, C_L and σ, a fair assessment on the scale effects can be performed in the subsequent sections.

Table 3: C_L at wetted flow condition

Grid	Model scale	Difference	Full scale	Difference
G1	0.440	-3.49%	0.456	-0.1 %
G2	0.441	-3.31%	0.456	0.1 %
G3	0.441	-3.18%	0.457	0.23 %
G4	-	-	0.452	-0.87 %
Exp. (TU Delft)	0.456			
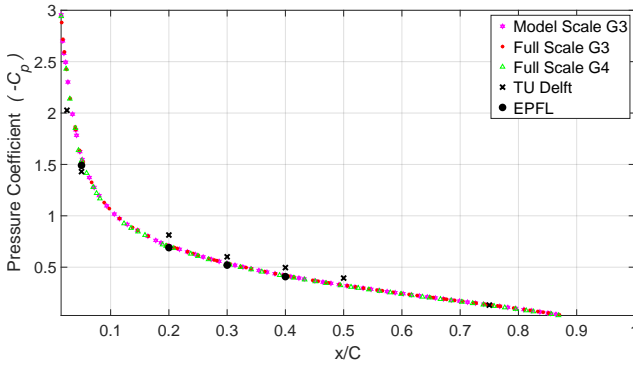
(a) 40% span

(b) 50% span

Figure 3: Predicted wetted flow pressure coefficient distribution at 40% span (top) and 50% span (bottom) along with experimental data.

Table 4: Components of C_D at wetted flow condition

	Model scale		Full scale	
Grid	Pressure	Shear	Pressure	Shear
G1	0.056	0.067	0.047	0.041
G2	0.052	0.070	0.043	0.044
G3	0.050	0.071	0.041	0.045
G4	-	-	0.045	0.046

Table 4 shows the predicted drag coefficient decomposed into its pressure and friction components for both model and full scales. The total drag coefficient at full scale is lower, and this is attributed to the difference in Reynolds numbers at which the viscous forces are more dominant at

model scale. Analyzing the components of C_D, one can also observe a change in the contributions of the pressure and shear components to the total drag depending on the grid resolution. At model scale, the predicted shear component is more dominant in all the grids and contributes to approximately 55% to 59% depending on the grid resolution. On the other hand, the predicted full scale drag components distribution is more sensitive to the grid resolution. G1 predicts the pressure component to be more dominant, while the opposite is predicted for finer grids (G2 & G3). While the mean y^+ is similar to the other finer grids, this indicates that the surface resolution is not sufficient in the coarsest grid. Also, the contribution from each component to the total drag is more balanced at full scale as predicted by G3 where the shear component contributes to only approximately 52%. G4 (wall function) provides a satisfactory prediction for the shear component relative to G3 but overpredicts the pressure component by approximately 10% relative to the finest grid.

4.2 Cavitating flow

4.2.1 Pressure Distribution

Figure 4 shows the numerically predicted averaged pressure coefficient distribution over multiple shedding cycles along with the experimental measurements at TU Delft and EPFL. Acceptable agreement with slight underprediction is obtained by the numerical results and the EPFL measurements while significant underprediction relative to the TU Delft data is present.

The results highlight the impact of surface and wall normal resolution, which is mutually dependent on the wall treatment as well. Near the leading edge $x/C < 0.1$ at the mid span location, the coarse grid G1 yields a slightly worse prediction in comparison to the finer grids and experiments. Since G1 has similar mean y^+ to finest grids, it indicates to the influence of the surface mesh resolution in this region. In addition, comparing G2 and G4 highlights the influence of wall normal grid resolution and boundary treatment. Although G2 and G4 have the same surface resolution, G4 with wall function predicts a worse pressure distribution. On the other hand, such differences are not as pronounced at the 0.4 spanwise location where the local angle of attack is smaller with lower pressure gradient.

In the region near the cavity closure, $0.3 < x/C < 0.45$, the wall function approach predicts very similar pressure distribution to G3 and G2. This indicates that the cavity length in the chord direction will also be of similar magnitude. Here, the resolution is important to capture the vortical structures and their interaction with the transported cloud cavity. This is further supported when looking at the predicted pressure distribution for the coarse grid G1. A worse prediction is obtained here as the coarse grid does not resolve the small-scale structures with sufficient quality. Also, numerical diffusion is mitigated with higher grid resolution which helps maintain the vortices as they travel in the downstream direction. Finally, at the cavity closure region where $0.45 < x/C < 0.55$, higher pressure is obtained with finer grids. This region is influenced by both

(a) Model scale 40% span

(b) Full scale 40% span

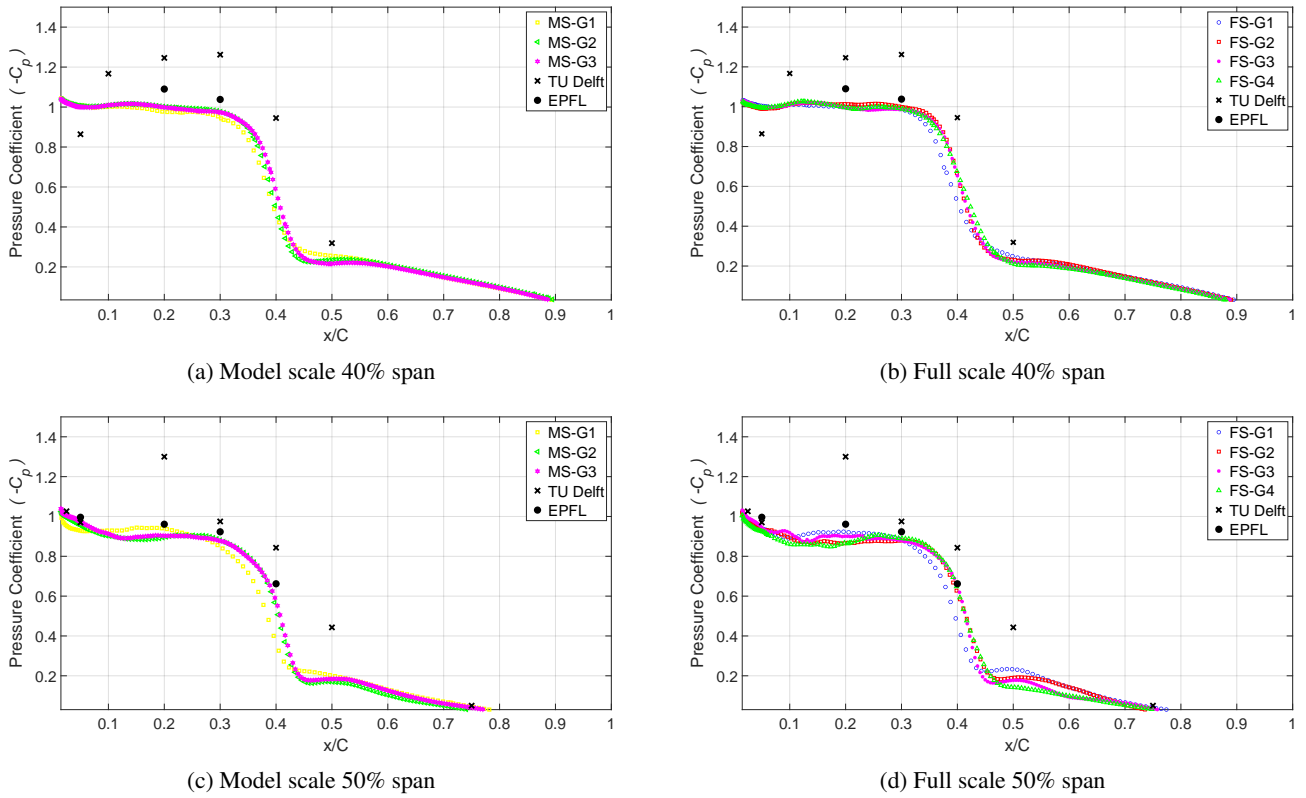(c) Model scale 50% span

(d) Full scale 50% span

Figure 4: Predicted wetted flow pressure coefficient distribution at 40% span (top) and 50% span (bottom) along with experimental data.

wall-normal and surface resolution. In this case, grids have similar wall normal resolution when the boundary layer is resolved, but further surface refinement predicts higher pressure as similarly observed by (Asnaghi *et al.*, 2018).

4.2.2 Lift and Drag Coefficient

Table 5 presents numerical predictions of the mean lift coefficient for model and full scale conditions, along with the experimental measurement. All grids underpredict the lift coefficient in comparison with the experimental data by more than 11%. In wetted flow condition, the same grids showed notably better agreement with the experiments. Such large discrepancy is attributed to the overprediction of the pressure distribution along the foil suction side surface shown in Figure 4 across the different grids.

Table 5: C_L at cavitating flow condition

Grid	Model scale	Difference	Full scale	Difference
G1	0.438	-14.8%	0.447	-12.3%
G2	0.443	-13.2%	0.450	-11.75%
G3	0.444	-12.9%	0.450	-11.73 %
G4	-	-	0.448	-12.2 %
Exp. (TU Delft)		0.456		

Table 6 shows the pressure and shear components of the drag coefficient at the model and full scales. In comparison with the wetted flow condition, the pressure component of drag is significantly increased making it the more dominant component. In fact, the pressure component now

contributes to more than 72% of the total drag. Such increase is explained by the low in pressure inside the cavity which also drives the main flow to re-circulate and split to form the re-entrant jet. In addition, the shear component of drag is reduced by the re-entrant jet flowing in the opposite direction of the main flow as well as the low shear in the vapor region. Finally, G4 with wall function approach gives results for the components of drag that are in good agreement with the finer grids.

Table 6: Components of C_D at cavitating flow condition

Grid	Model scale		Full scale	
	Pressure	Shear	Pressure	Shear
G1	0.158	0.056	0.160	0.034
G2	0.156	0.058	0.158	0.036
G3	0.154	0.059	0.157	0.037
G4	-	-	0.156	0.038

4.2.3 Cavitation Pattern and Shedding Behaviour

Analysis of the cavity pattern and shedding behavior is provided at different time instants in one typical shedding cycle T. The figures show the predicted cavity for the finest grids at both model and full scale conditions. It is visualized with an iso-surface for the volume fraction of vapor $\alpha_v = 0.5$, along with the normalized Q-criterion, Q^*, colored by vorticity. Q^* is calculated as $\frac{Q}{U_\infty/c^2}$, where c and U_∞ are the chord and free-stream velocity. The constrained streamlines of the wall shear stress are also shown in yel-

low.

A typical example for the shedding behavior of a partial/attached cavity is the instability that is driven by the re-entrant jet. As the attached cavity develops, the pressure gradient drives the main flow to curve toward the closure region and separates into two main components. The first component is what's called the re-entrant jet which travels in the opposite direction and toward the leading edge, while the second component re-attaches itself to the foil surface downstream of the closure region. When the re-entrant jet nears the leading edge, this initiates the break-off/detachment of the attached cavity and turns into a cloud that travels in the downstream direction.

In the case of the TU Delft Twist 11 foil, the re-entrant jet has two components (Foeth, 2008). The first part includes the component of the jet that travels in the upstream direction and perpendicular to the cavity closure. While the other component is given the name the side-entrant jet, which is driven into the sides of the sheet cavity. Although it also travels upstream toward the leading edge, the side-entrant jet is characterized by a strong spanwise velocity component.

The side re-entrant jet can be visualized in the first snapshot shown in Figure 5. Similar to the experiments, it is well predicted at this instant by the numerical model for both scales. Looking at the iso-surface of the Q^*, in proximity to the side-entrant jet, the region is rich with small-scale vortical structures that remove vapor content from the attached sheet and entrain them in the downstream direction. The volume of the entrained vapor is underpredicted by the numerical models which could be attributed to spatial resolution. In addition, a cloud structure appears downstream of the cavity closure. While it is not clear in this snapshot from the experiments, the numerical models predict the cloud to have a horse-shoe vortex structure. This can be clearly seen for both model and full scale conditions. However, one difference is the intermittent cavity structure at full scale for this horse-shoe vortex. It appears weaker based on the non-dimensional vorticity which induces higher pressure levels at the vortex core. Therefore, in our full scale simulations, the cloud tends to collapse at a relatively earlier stage during the shedding cycle.

Figure 6 shows a comparison of the predicted sheet cavity detachment at both scales. As mentioned previously, the re-entrant jet is responsible for the separation of the attachment from the surface as it nears the foil's leading edge. Comparing the results at model and full scale, two main differences are observed. First, the time instant at which the detachment occurs is not the same. At 0.3T of the full scale condition, the side and re-entrant jet components have reached to the leading edge and caused the cavity to separate from the surface of the foil. On the other hand, for that same time instant at model scale, while the side-entrant has reached the leading edge, the re-entrant jet does not initiate the detachment yet. In fact, the cavity detaches at approximately 0.4T for the model scale case. One explanation is that the jet momentum appears higher at full scale; further details on this are provided in the next section. The second

difference comes from detachment length in the spanwise direction. Comparing the instances at which the cavity separates, the detachment length in the spanwise direction at full scale appears shorter and more compact. It is still unclear as to why this behavior occurs, and more detailed investigation is needed.

After the main/side components of the jet reach the leading edge, the cavity is detached, and a traveling cloud structure is formed as shown in Figure 7. The top row shows a snapshot of the predicted cloud just after detachment at 0.6T. The cloud is characterized by a spanwise rolling vortex structure at both scales. In addition to this structure, a secondary vortex with its axis of rotation in the wall-normal direction starts to develop as well. While the strength of the spanwise vortex appears similar at both scales, the latter is weaker and thinner at full scale. This is evident by the smaller and thinner cavity structure within that vortex at the full scale condition.

This wall-normal vortex then evolves into a horse-shoe structure that carries a cavity within its core. This can be seen in the next snapshot at 0.8T. At this instant, the spanwise vortex has diminished and appears similar at both scales. On the other hand, the horse-shoe vortex appears weaker at full scale. The cavity structure looks thinner and less compact. As a result, it dissipates at a faster rate as shown in the next time instant at 1.0T. It appears that the vortex is too weak to maintain the cavity structure as it is transported in the downstream direction. While the cloud is being transported, a newly attached cavity develops to continue the shedding cycles.

Table 7: Predicted shedding frequency and Strouhal number at model and full scale

Grid	Model scale		Full scale	
	f	S_t	f	S_t
G1	31.5	0.678	1.67	0.626
G2	32.6	0.702	1.67	0.626
G3	32.6	0.702	1.67	0.626
G4	-	-	1.67	0.626
Exp. (TU Delft)	32.5	0.699		

To identify the shedding frequency of the cloud, the Fast Fourier Transform FFT is applied to the collected data of the cavitation volume over time. The FFT is applied on 30 and 6 shedding cycles for the model and full scale condition, respectively. The dominant frequency i.e. shedding frequency along with the Strouhal number for the different grids is shown in Table 7. The characteristic length is taken to be chord of the foil in the computation of the Strouhal number. Good agreement to the experiments is obtained especially with G2 and G3 where the relative difference is below 0.5%. While grid refinement provides better prediction at the model scale, it does not influence the predicted shedding frequency at full scale. In addition, when comparing the Strouhal number, different values are obtained for both scales. This indicates to a change in the re-entrant jet behavior from model to full scale, and will be further explored in the subsequent section of this paper.
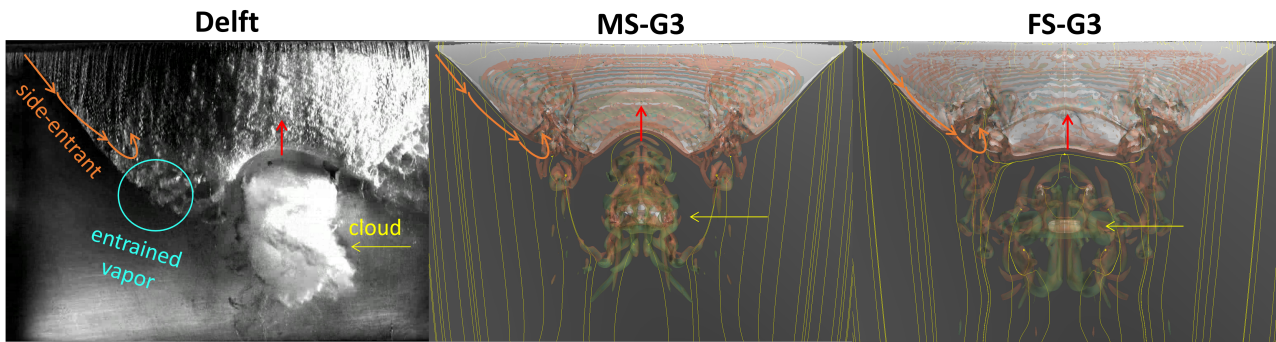
Figure 5: Comparison between the model scale (middle) and full scale (right) predicted cavity at 0.0 T for the finest grids G3, along with instantaneous snapshots of the experiments (left); cavitation is visualized with an iso-surface $\alpha = 0.5$; vortical structures are visualized with the normalized Q-criterion colored by non-dimensional vorticity.
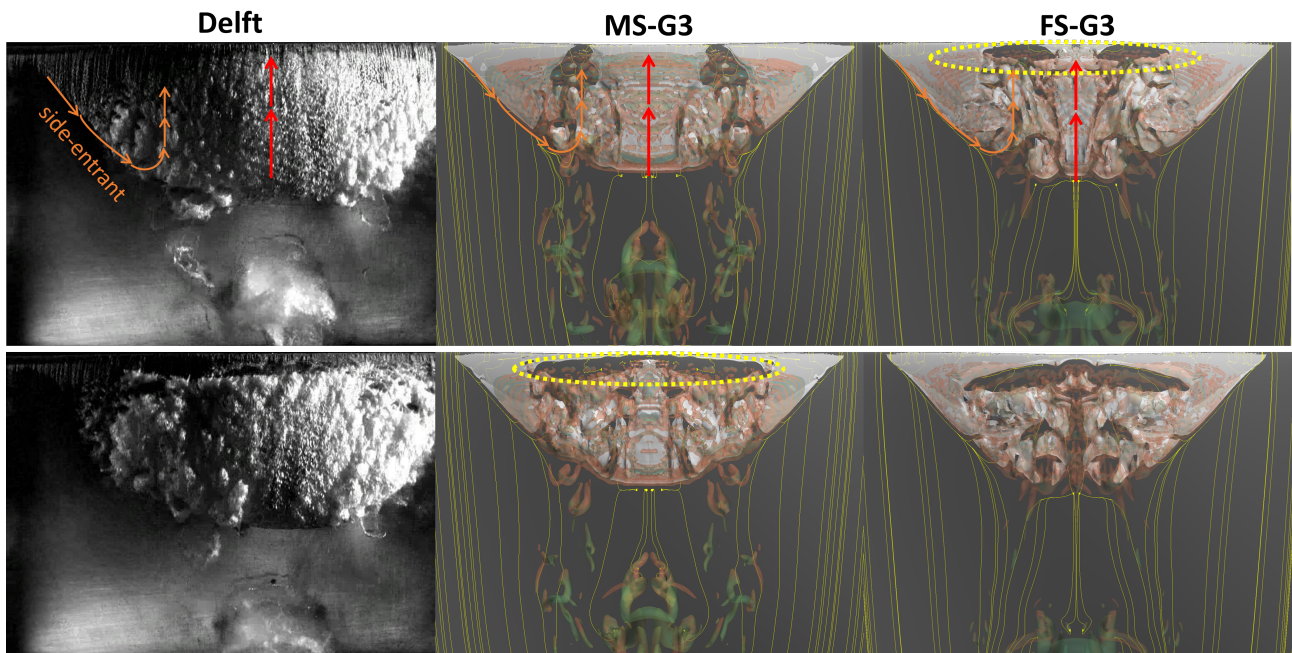

Figure 6: Comparison between the model (middle) and full scale (right) predicted cavity at 0.3T and 0.4T for the finest grids G3, along with instantaneous snapshots of the experiments; cavitation is visualized with an iso-surface $\alpha = 0.5$; vortical structures are visualized with the normalized Q-criterion colored by non-dimensional vorticity.

4.2.4 Re-entrant Jet

Here, the scale effects on the re-entrant jet are presented. Figure 8 shows the time evolution of the re-entrant jet at the midplane section for model scale (top), full scale G3 (middle), and full scale with the wall function approach G4 (bottom). The mid-plane is colored by the wall distance, and the cavity pattern is shown in grey.

The first instant at 0.0T shows the time at which the re-entrant jet just started making its journey toward the leading edge. Speaking in relative terms, the thickness of the cavity and re-entrant jet at both scales seem to be quite similar near the closure region. However, with the wall function approach, a thin liquid film is observed in the up-stream direction. Overall the maximum jet thickness is approximately 20% of the maximum cavity thickness. As it starts moving upstream as shown at 0.1T, the jet thickness at model scale appears to be diminishing rapidly which in-

dicates a considerable loss in momentum. On the other hand, it is maintained at full scale as predicted with both approaches of resolving the boundary layer (G3) or with the wall function approach (G4). At 0.2T, the same observation about momentum loss at model scale can be said, all the while the jet is steadily moving upstream at the full scale condition. In the last presented time instant at 0.3T, the cavity has detached at full scale and is about to begin its rolling in the downstream direction. However, at model scale, it is interesting to see that the jet seems to have stalled from the previous time instant and is unable to break the attachment at this moment in time. Although it eventually detaches just after, clearly the jet has lost significant momentum before managing to do so. The hypothesis to the greater loss of momentum at model scale is attributed to the greater frictional losses at model scale. The smaller Reynolds number would result in a relatively thicker boundary layer, hence
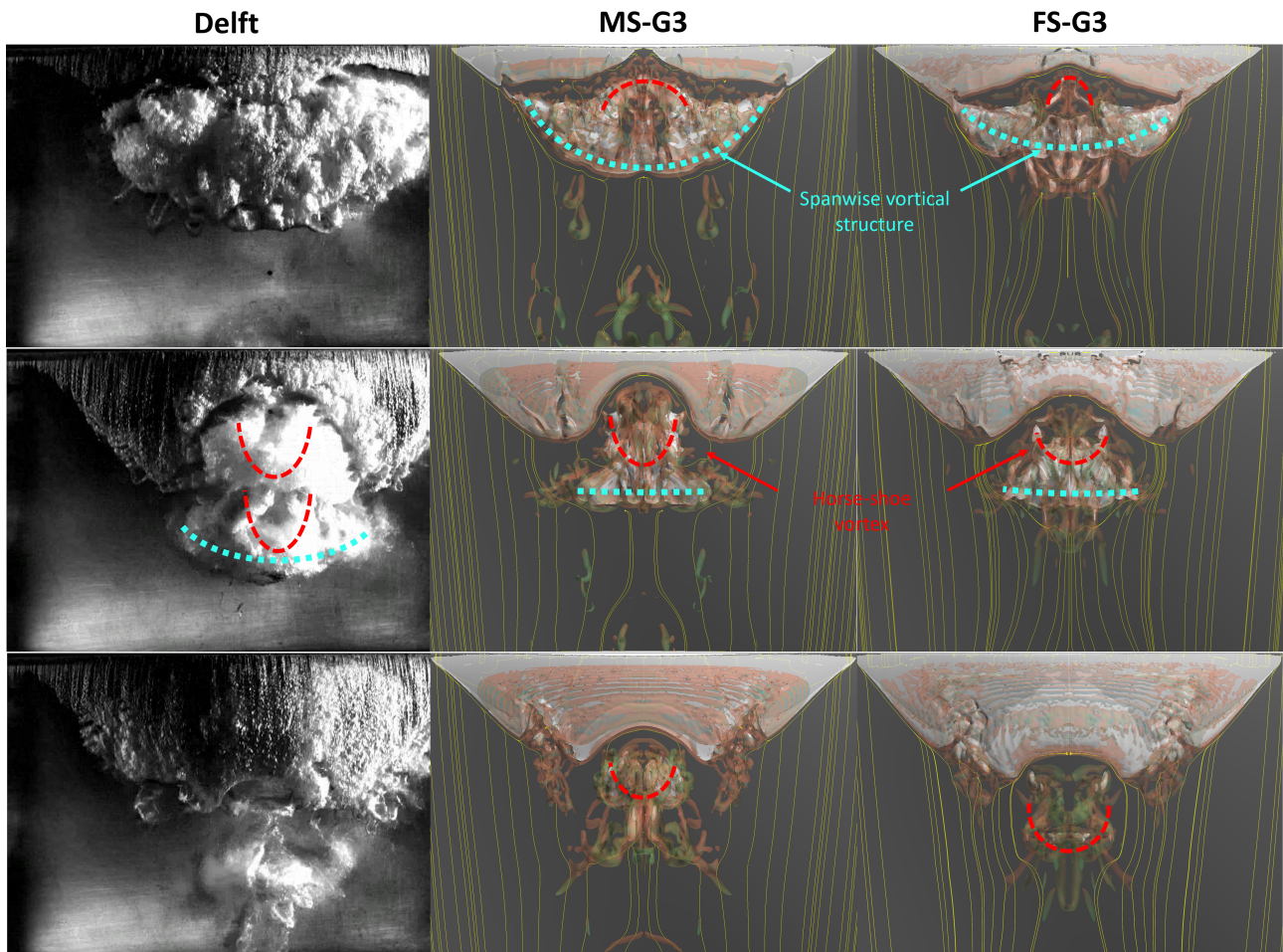
Figure 7: Comparison between the model (middle) and full scale (right) predicted cavity at 0.6T, 0.8T, 1.0T for the finest grids G3, along with instantaneous snapshots of the experiments; cavitation is visualized with an iso-surface $\alpha = 0.5$; vortical structures are visualized with the normalized Q-criterion colored by non-dimensional vorticity.

affecting the re-entrant jet as it travels upstream.

To gain a better insight into the scale effects on the re-entrant jet, the instantaneous non-dimensional velocity is plotted with the non-dimensional wall-normal distance as shown in Figure 9. Here, the velocity and wall distance are non-dimensionalized by the free stream velocity and chord length.

Looking at the velocity profile at $0.3\,C$ shown on the left side of Figure 9, the jet velocity is of the same magnitude as the free stream velocity. However, the profile at full scale is much fuller. This is not as pronounced with the wall function approach, but a similar profile can be seen. Moving closer the leading edge at $0.2\,C$ shown on the right side, significant differences are present. At model scale, the jet thickness has diminished more in comparison with the full scale condition. As stated earlier, this is an indication in significant momentum loss as the jet approached the leading edge of the the foil which explains the stalling behaviour and the delay in the detachment. On the other hand, the jet maintains a big part of its thickness at full scale, with differences in the velocity magnitude when using the wall function approach. Nonetheless, this does not

appear to impact the shedding frequency.

5 CONCLUSION

In this work, a study on the scale effects is presented for the TU Delft Twist 11 hydrofoil. Comparison and analysis are performed on the foil performance, pressure distribution, cavitation shedding, and behavior of the re-entrant jet. Regarding the cavitation shedding, it was observed that the scale effects have an influence on the secondary vortices that interact with the cavity structures. These vortices appear weaker at full scale which results in intermittent cavitation that dissipates at a higher rate in comparison with model scale results. In addition, the analysis of the re-entrant jet reveals differences between both scales. It appears that the jet is relatively thicker at full scale, and maintains its momentum as it travels toward the leading edge. This was also well captured with the wall function approach, but the jet appears slightly thinner relative to the observation made when resolving the boundary layer. In contrast, significant momentum loss is clearly present at model scale which causes the re-entrant jet to stall before breaking the attached cavity.

REFERENCES

Asnaghi, A., Bensow, R. E. (2020). Impact of leading edge roughness in cavitation simulations around a twisted foil. Fluids, **5**(4), pp. 243.

Asnaghi, A., Feymark, A., & Bensow, R. (2018). Numerical investigation of the impact of computational resolution on shedding cavity structures. International Journal of Multiphase Flow, **107**, pp. 33-50.

Bark, G., Grekula, M., Bensow, R., & Berchiche, N. (2009). On some physics to consider in numerical simulation of erosive cavitation. Proceedings of the International Symposium on Cavitation Michigan, USA.

Bensow, R. E. (2011). Simulation of the unsteady cavitation on the TU Delft Twist11 foil using RANS, DES and LES. Second international symposium on marine propulsors Hamburg, Germany.

Coutier-Delgosha, O., Fortes-Patella, R., & Reboud, J. L. (2003). Evaluation of the turbulence model influence on the numerical simulations of unsteady cavitation. *J. Fluids Eng.,* **125**(1), 38-45.

Crepier, P. (2017). Ship resistance prediction: verification and validation exercise on unstructured grids. International conference on computational in marine engineering, Nantes, France.

Foeth, E. (2008). The Structure of Three-Dimensional Sheet Cavitation (Ph. D. thesis). TU Delft University of Technology, The Netherlands.

Franc, J. P., & Michel, J. M (1985). Attached cavitationand the boundary layer: experimental investigation and numerical treatment. Journal of Fluid Mechanics, **154**, pp. 63–90.

Menter, F.R., Kuntz, M., & Langtry, R. Ten years of industrial experience with the SST turbulence model. Turbulence, heat and mass transfer, **4**, pp. 625–632

Reboud, J. L., Stutz, B., & Coutier, O. (1998). Two-phase flow structure of cavitation: experiment and modeling of unsteady effects. In *3rd International Symposium on Cavitation, Grenoble, France* (Vol. 26, pp. 1-8).

Schnerr, G. H., & Sauer, J. (2001). Physical and numerical modeling of unsteady cavitation dynamics. Fourth international conference on multiphase flow, New Orleans, USA.

Schultz, M. P., & Flack, K. A. (2007). The rough-wall turbulent boundary layer from the hydraulically smooth to the fully rough regime. Journal of Fluid Mechanics,, **580**, pp. 381–405.

Whitworth, S. (2011). Cavitation prediction of flow over the TU Delft twist 11 foil. Second international symposium on marine propulsors, Hamburg, Germany.
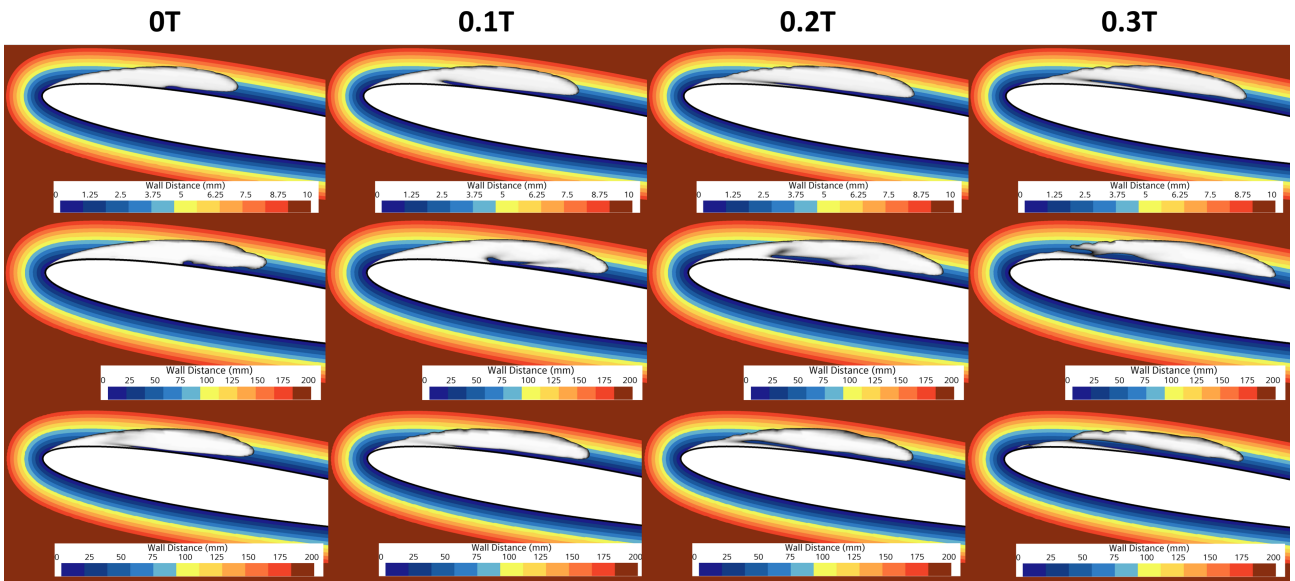
Figure 8: Visualization of the cavity and re-entrant jet thickness and time evolution for model scale G3 (top), full scale G3 (middle), and full scale with the wall function approach G4 (bottom).
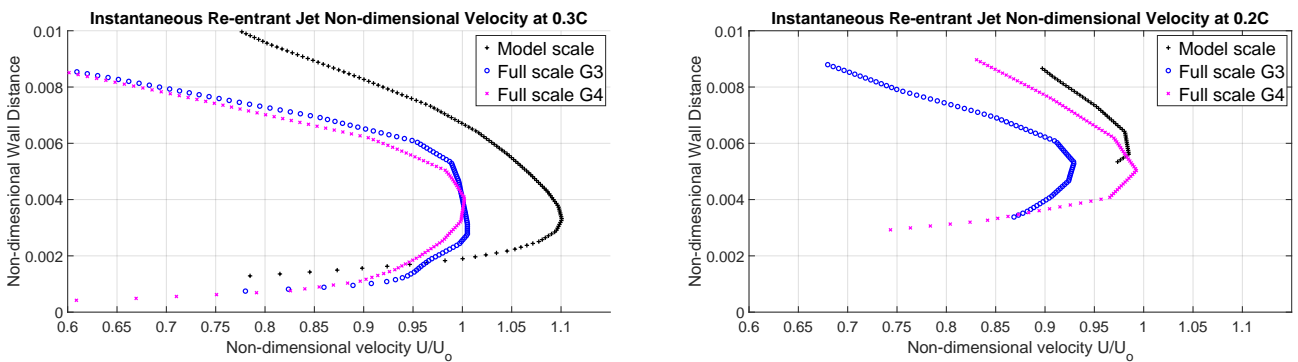

Figure 9: Instantaneous plots of the re-entrant jet non-dimensional velocity with respect to the non-dimensional wall-normal distance at 0.2 and 0.3 of the chord length